

# Deuterium labeling enables non-invasive 3D proton MR imaging of glucose and neurotransmitter metabolism in the human brain

**Petr Bednarik**

High-Field MR Center, Department of Biomedical Imaging and Image-Guided Therapy  
<https://orcid.org/0000-0002-8828-7661>

**Dario Goranovic**

High-Field MR Center, Department of Biomedical Imaging and Image-Guided Therapy

**Alena Svátková**

Medical University of Vienna

**Fabian Niess**

Medicao University of Vienna

**Lukas Hingerl**

High-Field MR Center, Department of Biomedical Imaging and Image-Guided Therapy

**Bernhard Strasser**

A. A. Martinos Center for Biomedical Imaging, Massachusetts General Hospital <https://orcid.org/0000-0001-9542-3855>

**Dinesh Deelchand**

Center for Magnetic Resonance Research, University of Minnesota

**Benjamin Spurny-Dworak**

Medical University of Vienna

**Siegfried Trattinig**

High-Field MR Center, Department of Biomedical Imaging and Image-Guided Therapy

**Gilbert Hangel**

High-Field MR Center, Department of Biomedical Imaging and Image-Guided Therapy  
<https://orcid.org/0000-0002-3986-3159>

**Thomas Scherer**

Department of Medicine III, Medical University of Vienna

**Rupert Lanzenberger**

Medical University of Vienna <https://orcid.org/0000-0003-4641-9539>

**Wolfgang Bogner** (✉ [wolfgang.bogner@meduniwien.ac.at](mailto:wolfgang.bogner@meduniwien.ac.at))

High-Field MR Center, Department of Biomedical Imaging and Image-Guided Therapy

**Keywords:**

**Posted Date:** December 6th, 2021

**DOI:** <https://doi.org/10.21203/rs.3.rs-1027370/v1>

**License:**   This work is licensed under a Creative Commons Attribution 4.0 International License.

[Read Full License](#)

---

# 1 Deuterium labeling enables non-invasive 3D proton MR imaging of 2 glucose and neurotransmitter metabolism in the human brain

3  
4 Petr Bednarik<sup>1</sup>, Dario Goranovic<sup>1</sup>, Alena Svatkova<sup>2</sup>, Fabian Niess<sup>1</sup>, Lukas Hingerl<sup>1</sup>, Bernhard  
5 Strasser<sup>1</sup>, Dinesh Deelchand<sup>3</sup>, Benjamin Spurny-Dworak<sup>4</sup>, Siegfried Trattnig<sup>1</sup>, Gilbert  
6 Hangel<sup>1,5</sup>, Thomas Scherer<sup>2</sup>, Rupert Lanzenberger<sup>4</sup>, Wolfgang Bogner<sup>1</sup>

7  
8 1 High-Field MR Centre, Department of Biomedical Imaging and Image-Guided Therapy, Medical University of  
9 Vienna, Vienna, Austria

10 2 Department of Medicine III, Clinical Division of Endocrinology and Metabolism, Medical University of Vienna,  
11 Vienna, Austria

12 3 Center for Magnetic Resonance Research, University of Minnesota, Minneapolis, USA

13 4 Department of Psychiatry and Psychotherapy, Medical University of Vienna, Vienna, Austria

14 5 Department of Neurosurgery, Medical University of Vienna, Vienna, Austria

## 15 16 **Correspondence to:**

17  
18 Wolfgang Bogner, Ph.D.

19 [wolfgang.bogner@meduniwien.ac.at](mailto:wolfgang.bogner@meduniwien.ac.at)

20 Phone: +43 676 9138356

21  
22 Petr Bednarik, MD, Ph.D.

23 [pbed.radiol@gmail.com](mailto:pbed.radiol@gmail.com)

24 Phone: +43 664 75357588

## 25 26 27 **Abstract**

28  
29 Impaired brain glucose metabolism characterizes most severe brain diseases. Recent  
30 studies have proposed deuterium (<sup>2</sup>H)-Magnetic Resonance Spectroscopic Imaging (MRSI)  
31 as a reliable, non-invasive, and safe method to quantify the human metabolism of <sup>2</sup>H-labeled  
32 substrates such as glucose and their downstream metabolism (e.g., aerobic/anaerobic  
33 glucose utilization and neurotransmitter synthesis) and address the major drawbacks of  
34 positron emission tomography (PET) or carbon (<sup>13</sup>C)-MRS. Here, for the first time, we show  
35 an indirect dynamic proton (<sup>1</sup>H)-MRSI technique in humans, which overcomes four critical  
36 <sup>2</sup>H-MRSI limitations. Our innovative approach provides higher sensitivity with improved  
37 spatial/temporal resolution and higher chemical specificity to differentiate glutamate (Glu<sub>4</sub>),  
38 glutamine (Gln<sub>4</sub>), and gamma-aminobutyric acid (GABA<sub>2</sub>) deuterated at specific molecular  
39 positions while allowing simultaneous mapping of both labeled and unlabeled metabolites  
40 without the need for specialized hardware. Our novel method demonstrated significant Glu<sub>4</sub>,  
41 Gln<sub>4</sub>, and GABA<sub>2</sub> decreases, with 18% faster Glu<sub>4</sub> reduction in the gray matter than white  
42 matter after ingestion of deuterated glucose. Thus, robustly detected downstream glucose  
43 metabolism utilizing clinically available MR hardware without the need for radioactive tracers  
44 and PET.

45 **Introduction (683 words)**

46

47 Non-invasive, affordable, and reliable mapping of glucose metabolism in the human brain is  
48 critically needed for both clinical and neuroscientific studies. While current approaches, such  
49 as fluorodeoxyglucose ( $[^{18}\text{F}]\text{FDG}$ ) positron emission tomography (PET), carbon-13 ( $^{13}\text{C}$ )  
50 magnetic resonance spectroscopy ( $^{13}\text{C}$ -MRS), and direct deuterium magnetic resonance  
51 spectroscopic imaging ( $^2\text{H}$ -MRSI) of glucose metabolism, are technically challenging and  
52 require special hardware or expensive synthesis of intravenous radioactive tracers, a recent  
53 animal study has shown the incredible potential for the indirect detection of deuterated  
54 compounds via proton magnetic resonance spectroscopy ( $^1\text{H}$ -MRS) to quantify glucose  
55 metabolism in the rat brain.<sup>1</sup> Orally administered, deuterium-labeled glucose is readily taken  
56 up by brain cells, and the deuterons are incorporated into downstream glucose metabolites.<sup>2</sup>  
57 Since deuterons ( $^2\text{H}$ ) substitute protons ( $^1\text{H}$ ) in the molecule ( $^2\text{H}$ -to- $^1\text{H}$ -MRS), they do not  
58 contribute to the proton ( $^1\text{H}$ ) spectrum. Hence, the increase in deuterium-labeled metabolites  
59 is reflected by the decrease in metabolite signals in  $^1\text{H}$ -MRS.

60

61 About ninety-five percent of the glucose in the healthy brain enters the tricarboxylic acid  
62 (TCA) cycle for glutamate cycling. The rest converts anaerobically to lactate (Lac).<sup>3</sup>  
63 Glutamate (Glu) is then involved in the glutamate/glutamine cycle, ammonia detoxification,  
64 and GABA synthesis to supply excitatory and inhibitory neurotransmitters. The balance  
65 between aerobic and anaerobic glycolysis is critical for maintaining brain homeostasis, and  
66 the shift from healthy aerobic glucose (Glc) metabolism to anaerobic pathways (i.e., Warburg  
67 effect) characterizes pathological conditions seen in tumors and ischemia.<sup>4</sup> Anaerobic  
68 metabolism also plays a crucial role in mitochondrial dysfunction, a critical early condition in  
69 the pathophysiology of severe neurological diseases, such as Alzheimer's disease<sup>5</sup> and  
70 neuropsychiatric disorders such as major depression and schizophrenia.<sup>6</sup>

71

72 The gold standard for the clinical examination of metabolism, i.e., positron emission  
73 tomography (PET), with the glucose analog  $^{18}\text{F}$ -fluorodeoxyglucose ( $[^{18}\text{F}]\text{FDG}$ ) indeed  
74 provides quantitative measurements of the cerebral metabolic rate of Glc ( $\text{CMR}_{\text{Glc}}$ ). However,  
75  $[^{18}\text{F}]\text{FDG}$  is metabolically inert and, thus, cannot assess downstream metabolism, which is  
76 relevant for diagnosis and treatment evaluation.<sup>7,8</sup>  $^{13}\text{C}$ -MRS is a research tool, which can  
77 quantify these compounds of the brain's cycles;<sup>8</sup> although the method suffers from poor  
78 spatial localization. Hyperpolarized carbon-13 ( $^{13}\text{C}$ )-MRSI is another emerging molecular  
79 MRI method for rapid, pathway-specific investigation of dynamic metabolic and physiologic

80 processes and is not yet available in the clinical setting.<sup>9</sup> The power of hyperpolarized <sup>13</sup>C-  
81 MRSI lies in its ability to investigate the entire metabolic pathway, including downstream  
82 metabolites, which is not possible via [<sup>18</sup>F]FDG PET. However, currently, the widely used  
83 substance, i.e., <sup>13</sup>C1-labeled pyruvate, mainly measures the conversion rate of pyruvate to  
84 lactate, while it does not provide information about other metabolic pathways. Both PET and  
85 hyperpolarized <sup>13</sup>C-MRSI require additional costly hardware and invasive intravenous  
86 substrate administration, with PET also requiring harmful radioactive and unstable tracers.

87

88 Recently, direct <sup>2</sup>H-MRS detection provided alternative measures to address the  
89 aerobic/anaerobic imbalance, but the technique requires special hardware and estimates  
90 only a limited number of deuterated compounds, which diminishes its clinical applicability. In  
91 contrast, the proposed <sup>2</sup>H-to-<sup>1</sup>H-MRS promises to overcome these limitations by utilizing  
92 harmless and stable tracers and allowing quantification of both cerebral metabolic rates of  
93 Glc (CMRGlc) as well as the turnover of downstream intracellular Glc metabolism.<sup>1</sup>

94

95 Thus, since the deuterium method enables quantification of both the oxidative and anaerobic  
96 glucose utilization and assesses neurotransmitter synthesis, we aimed to establish, for the  
97 first time, non-invasive detection of deuterium enrichment after peroral administration of 6,6'-  
98 <sup>2</sup>H<sub>2</sub>-Glc (Deu-Glc) using <sup>1</sup>H-MRS in the healthy human brain. Compared to direct <sup>2</sup>H-MRS  
99 detection, the indirect technique allows quantification of extended metabolic profiles while  
100 reliably reflecting downstream metabolism, as shown in a single animal study.<sup>1</sup> Motivated by  
101 the desire to establish a novel, easy-to-apply approach for metabolic mapping in humans, we  
102 employed state-of-the-art methods of single-voxel <sup>1</sup>H-MRS<sup>10</sup> and echo-less 3D <sup>1</sup>H-MRSI,<sup>11</sup>  
103 which have previously demonstrated high sensitivity for the detection of small functional  
104 responses to physiological stimulation.<sup>12,13</sup> Our current objective was to trace and map the  
105 decaying metabolite signals after non-invasive oral administration of deuterated Glc, utilizing  
106 widely available hardware. The experiments were conducted in two sessions with either  
107 deuterated Glc (Deu-Glc) or non-deuterated Glc (normal dextrose, nonDeu-Glc) ingestion to  
108 mitigate the possible metabolic effects of the Glc load, particularly those of hyperglycemia  
109 and insulin release.<sup>14</sup>

110

111

112

113

114

115 **Methods (1644 words):**

116

117 **Study design**

118

119 Five healthy, right-handed volunteers (30±4 y.o., 5 males) were scanned on a 7T whole-body  
120 MR scanner (Siemens Healthcare, Erlangen, Germany) utilizing a 32-channel receive-array  
121 coil (Nova Medical, Wilmington, MA, USA). All participants were lean (BMI = 22.6±1.4 kg/m<sup>2</sup>)  
122 without a history of diabetes or other metabolic and severe diseases. The study was  
123 approved by the Ethical Commission at the Medical University of Vienna. All participants  
124 signed informed consent. Each participant underwent two MR scans, one after 6,6'-<sup>2</sup>H<sub>2</sub>-Glc  
125 (Deu-Glc), the other after non-deuterated D-Glc (normal dextrose, nonDeu-Glc)  
126 administration; the scans were 92±49 days apart. All these scans used an interleaved single-  
127 voxel MRS/MRSI protocol. One subject was additionally scanned after Deu-Glc  
128 administration with MRSI-only protocol to obtain the time-course with high temporal  
129 resolution. All sessions were conducted in the morning after an overnight fast. Both  
130 compounds were dissolved in ~300 mL of water and ingested in equal amounts (0.8 g/kg  
131 body weight) immediately before the scan was initiated. MRSI and MRS data were  
132 interleaved with navigator images obtained prior to each MRSI/MRS acquisition to assure the  
133 stable position of the localized volume. The navigator images were registered to the atlas  
134 space with Autoalign methodology implemented on the MR scanner.<sup>15</sup> The coordinates of the  
135 MRS volume of interests (MRS-VOI) were later used in the second MR session for consistent  
136 MRS-VOI placement. The first MRS/MRSI block was acquired after calibrating MRS RF-  
137 pulses and B<sub>0</sub>-shimming within 30 minutes after Deu-Glc/nonDeu-Glc administration. The  
138 following MRS/MRSI blocks were obtained after the acquisition of the T1-weighted  
139 MP2RAGE image with an isotropic resolution of 1.1×1.1×1.1 mm<sup>3</sup>; TR, 3900 ms; TE, 2.8 ms;  
140 flip angle, 4°/5°; acquisition time 3:52 min; and GRAPPA factor 4. Our goal was to cover a  
141 time window of 120 minutes following the ingestion of the tracer, assuming slower dynamics  
142 of deuterium enrichment in the human brain compared to that of rats.<sup>1</sup>

143

144 **MRI/MRS data acquisition**

145

146 Standard 2nd-order B<sub>0</sub>-shimming was performed via an imaging-based approach (two  
147 iterations) and FASTMAP<sup>16</sup> for MRSI and MRS acquisition, respectively. Multi-voxel (MRSI)  
148 and single-voxel (SV-MRS) acquisitions were interleaved except for one study session,

149 where only the MRSI data were acquired with a high time resolution of five minutes after Deu-  
150 Glc ingestion.

151 MRSI data were obtained via an FID-MRSI sequence<sup>11</sup> with an ultra-short acquisition delay  
152 of 1.3 ms, a short TR of 320 ms, and ellipsoidal 3D k-space encoding using concentric ring  
153 trajectories (CRT), variable temporal interleaves, 36x36x26 matrix, 5x5x4.8 mm<sup>3</sup> voxel size,  
154 2:58 min per block, 558 complex points, 34° (Ernst) excitation flip angle, 600 μs pulse  
155 duration, and 7 kHz pulse bandwidth. The excited slab was centered around the posterior  
156 cingulate region.

157 Single-voxel MRS data were obtained from the posterior cingulate (PCC) region using a semi-  
158 LASER sequence (TR 7 s, TE 28 ms, 3:43 min per block, 2048 complex points, 90°  
159 asymmetric sinc pulse with a duration of 2.5 ms, FOCI pulse bandwidth, and a duration of  
160 4.2 ms, 45 kHz).<sup>17</sup> A 22×20×20 mm (AP×LR×SI) voxel was placed mid-sagittally, based on  
161 anatomical landmarks. The voxel was rotated in the sagittal plane by 30° such that it was  
162 aligned with the posterior border of the splenium. To mitigate possible effects of patient  
163 motion and chemical shift displacement, the voxel was backed away anteriorly from the  
164 splenium and caudally from the occipital-parietal fissure by 2 mm.<sup>18</sup> All spectra were collected  
165 with water suppression<sup>19</sup> and outer volume suppression (number of excitations, NEX = 32)  
166 along with unsuppressed water spectra utilized to remove residual eddy currents (NEX = 2)  
167 and as a reference from which to derive metabolite concentration estimates (NEX = 2).

168

### 169 **Segmentation of MPRAGE scans**

170

171 The T1w-MRI images were segmented in Freesurfer (v.5.3) to obtain masks of the brain gray  
172 matter (GM) and white matter (WM). The masks were resampled to the MRSI space and  
173 used to obtain tissue-specific averages of metabolite levels. In addition, probabilistic maps of  
174 the GM, WM, and cerebrospinal fluid (CSF) were derived by segmenting the T1w-MRI images  
175 using the SPM12 software package. The probabilistic tissue maps were thresholded with an  
176 in-house-written MATLAB script using the iterative method of threshold selection<sup>20</sup> to  
177 determine the within-PCC-VOI fraction of GM, WM, and CSF.

178

### 179 **Processing of MRSI**

180

181 MRSI data were reconstructed offline with an in-house-developed software pipeline<sup>21</sup>  
182 consisting of MATLAB (R2013a, MathWorks, Natick, MA, USA), BASH (v4.2.25, Free  
183 Software Foundation, Boston, MA, USA), and MINC (MINC tools, v2.0, McConnell Brain

184 Imaging Center, Montreal, QC, Canada). Data processing included an iMUSICAL coil  
185 combination,<sup>22,23</sup> water normalization,<sup>24</sup> k-space reconstruction with in-plane convolution  
186 gridding, spatial Hamming filtering, channel-wise noise-decorrelation, and off-resonance  
187 correction.<sup>25</sup> Due to the short TR, obtaining metabolite concentration estimates would require  
188 strong assumptions about  $T_1$  relaxation. Therefore, the metabolite concentrations were  
189 instead quantified in institutional units using LCModel (v6.3-1, LCModel Inc, ONT, CA) with  
190 a basis set that included 17 simulated brain metabolites and a measured macromolecular  
191 background (detailed below).<sup>26</sup>

192

### 193 **Processing of SV-MRS**

194

195 Single shots were corrected for small frequency and phase fluctuations, and residual eddy  
196 currents, and 32 single shots were summed per block. The frequency and phase of the  
197 spectra obtained for each block were aligned to each other within the scanning session and  
198 quantified in LCModel. The metabolite concentrations were corrected for variable water  
199 content in the gray and white matter, as well as for the within-voxel CSF fraction.<sup>27</sup>

200 Finally, the spectra representing the first time-points (FIRST) and the last time-points (LAST)  
201 were pooled together and summed, resulting in two sums (FIRST and LAST) for each session  
202 (Deu-Glc and nonDeu-Glc). The FIRST and LAST from the Deu-Glc session were subtracted,  
203 and a difference spectrum was calculated. The difference spectrum characterized metabolite  
204 changes following Deu-Glc ingestion. In addition, the LAST points from the two sessions  
205 (nonDeu-Glc and Deu-Glc) were subtracted. The difference spectrum represented the effect  
206 of deuterium enrichment without the possible metabolic effects of hyperglycemia, which were  
207 present in both sessions. The difference spectra were quantified in LCModel utilizing the  
208 basis sets that contained only the metabolites enriched with deuterium (detailed below) to  
209 estimate quantification errors, i.e., relative Cramer-Rao-Lower-Bounds (CRLB).<sup>28</sup>

210

### 211 **Quantification of MR spectra**

212

213 Basis sets previously routinely used to quantify  $^1\text{H}$ -MRS/MRSI data were modified to reflect  
214 the fact that deuterium is incorporated at certain carbon positions in the molecules.  
215 Modifications to the basis sets were performed based on the previous animal experiments,  
216 theoretical predictions, and preliminary analysis of the current data. Glu, Gln, and GABA  
217 included the split of proton signals that originated from different carbon positions for C2, C3,  
218 and C4. Thus, the basis set included all molecular variants that occurred in the brain in a

219 dynamically changing ratio and took into account the homonuclear ( $^1\text{H}$ - $^1\text{H}$ ) and heteronuclear  
220 ( $^1\text{H}$ - $^2\text{H}$ ) coupling constants. For instance, the basis set of glutamate included six components,  
221 i.e., those present in the molecule with all positions occupied with protons ( $\text{C}2^1\text{H}$ ,  $\text{C}3^1\text{H}_2$ ,  
222  $\text{C}4^1\text{H}_2$ ), in the molecule with one deuteron on the C4 ( $\text{C}2^1\text{H}$ ,  $\text{C}3^1\text{H}_2$ ,  $\text{C}4^1\text{H}^2\text{H}$ ), and two  
223 deuterons on C4 ( $\text{C}2^1\text{H}$ ,  $\text{C}3^1\text{H}_2$ ). Thus, we distinguished three variants of the C3 resonance  
224 affected by homo- and heteronuclear coupling with  $^1\text{H}$  and  $^2\text{H}$  at C4. While the couplings  
225 between protons and deuterons on the C3 and C4 (Glu and Gln) and C2 and C3 (GABA)  
226 were simulated, the couplings between C2 and C4 were minimal and were neglected. Yet,  
227 the number of components had to be reduced for MRS and MRSI data to preserve the stability  
228 of the fits. This was performed by neglecting the heteronuclear and homonuclear coupling  
229 effects of the deuteration, assuming that the dominant signal change occurred on the position  
230 where proton(s) is/are replaced by deuteron(s), i.e., C4 for Glu and Gln and C2 for GABA.  
231 Thus, we used only two components per metabolite ( $\text{Glu}_{2+3}$ ,  $\text{Glu}_4$ ;  $\text{Gln}_{2+3}$ ,  $\text{Gln}_4$ ; and  $\text{GABA}_2$ ,  
232  $\text{GABA}_{3+4}$ ) to quantify SV-MRS data. The basis set was further simplified for MRSI, where we  
233 split only  $\text{Glu}_{2+3}$  and  $\text{Glu}_4$  resonances since the fitting with more components yielded a less  
234 stable quantification of neurochemical profiles. Finally, we used the components whose  
235 signals were expected to change due to progressive deuteration during the scans (i.e., for  
236 Glu and Gln:  $\text{C}4^1\text{H}_2$ ,  $\text{C}4^1\text{H}^2\text{H}$  and two variants of  $\text{C}3^1\text{H}_2$  present in the molecule with and two  
237 deuterons; and for GABA:  $\text{C}2^1\text{H}_2$ ,  $\text{C}2^1\text{H}^2\text{H}$ , and two variants  $\text{C}3^1\text{H}_2$ ) to quantify the difference  
238 spectra. As difference spectra do not contain the background of signals from the metabolites  
239 that were stable over the task, we could account for the subtle hetero- and homonuclear  
240 coupling effects.

241

### 242 **Quality control of MRS(I) data**

243

244 Voxels with sufficient temporal stability and spectral quality were selected using masks. The  
245 masks included voxels with CVs below 12% for the three main metabolites that remained  
246 stable during the scan, i.e., tCr, tCho, and tNAA. The criteria also utilized parameters  
247 provided by LCModel (FWHM < 0.1 ppm, SNR > 5, zero-order phase < 40°) in line with expert  
248 recommendations.<sup>29</sup> These criteria were utilized to calculate regional GM and WM means in  
249 metabolite concentrations, as well as to select the spectra used for the calculation of high-  
250 SNR sums that represented either GM or WM. The metabolite concentrations quantified with  
251 all CRLBs were used for further analysis except those that could not be quantified with CRLBs  
252 of 999%. This criterion avoided bias due to an arbitrarily set CRLB threshold, cutting off lower  
253 concentrations with higher relative CRLB.<sup>30</sup> The metabolites quantified with a CRLB of 999%

254 in most of the time-points (MRS), or consistently in more than 10% of voxels (MRSI), were  
255 not analyzed.<sup>31</sup>

256

## 257 **Statistical analysis**

258

259 Differences in metabolite concentrations were calculated between the first and last time-  
260 point, and their significance was tested with the standard paired t-test separately within both  
261 sessions (Deu-Glc, nonDeu-Glc). Time-dependent decay in the Glu<sub>4</sub> concentration after Deu-  
262 Glc administration was fitted with an exponential function  $M=M_0e^{-t/\tau}+c$  per subject. The  
263 coefficient of variations in the time constants of the decay ( $\tau$ ) were calculated per session  
264 to express the between-subject variation of the metabolic rates between subjects in the  
265 region of interest (PCC, GM, WM). The concentrations of Gln<sub>4</sub> (both sessions) and Glu<sub>4</sub>  
266 (nonDeu-Glc) were instead fitted with linear functions ( $Y=slopes*t+a$ ).

267

268

269

270

271

272

273

274

275

276

277

278

279

280

281

282

283

284

285

286

287

288

289 **Results (863 words):**

290

291 **SV-MRS: time-course analysis**

292

293 While the signal amplitudes at the deuterated C4 position dropped for both Glu (Glu<sub>4</sub>) and  
294 Gln (Gln<sub>4</sub>) by 14.3% ± 2.0% (p = 0.00014) and 12.3% ± 4.5% (p=0.0019), respectively,  
295 following Deu-Glc ingestion in accord with previous animal data,<sup>1</sup> Glu<sub>4</sub> and Gln<sub>4</sub> were stable  
296 during the control experiment using the administration of nonDeu-Glc (Table 1, Fig.1). Asp,  
297 Glu<sub>2+3</sub>, Gln<sub>2+3</sub>, GABA<sub>2</sub>, GABA<sub>3+4</sub>, and Lac, as well as all other metabolites, did not change  
298 significantly during both sessions.

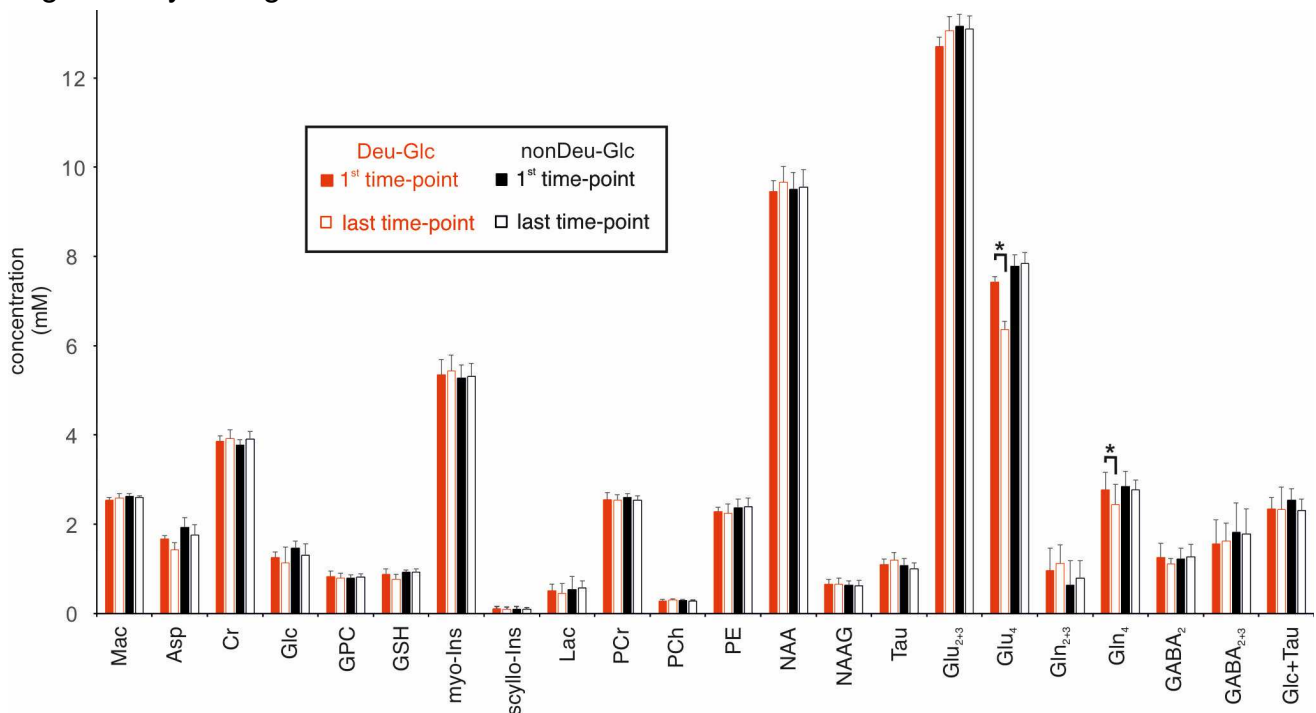


**Fig.1. Quantification of SV-MR spectra in LCModel.** Bar diagrams demonstrate means (errors bars represent standard error of the mean) of concentration comparisons quantified from the first and last time-point spectra following Deu-Glc and nonDeu-Glc administration. Peaks that originated from the specific carbon position undergoing deuteration, namely, the 4<sup>th</sup> carbon position for Glu (Glu<sub>4</sub>) and Gln (Gln<sub>4</sub>) and the 2<sup>nd</sup> carbon position for GABA (GABA<sub>2</sub>), were separated. Concentrations were compared with a standard, two-tailed, paired t-test between the first and last time-point within the Deu-Glc and nonDeu-Glc sessions.

299

300

301

302

303

304

305 The within-session average of Glc levels was  $0.33 \pm 0.2\text{mM}$  ( $p = 0.04$ ) lower during the Deu-  
 306 Glc scan than during the nonDeu-Glc session, reflecting the  $^1\text{H}$ -invisible signal from the  
 307 deuterated component of Deu-Glc. The Glc time-course gradually increased during the first  
 308 half of the experiment and returned to baseline values subsequently. As our experiment  
 309 resembled an oral glucose tolerance test, the time-course approximately reflects the glycemic  
 310 levels typical for healthy subjects. Changes in the signal of GABA and GABA<sub>2</sub> were not  
 311 statistically significant, possibly due to higher variance in GABA and GABA<sub>2</sub> typical for non-  
 312 edited  $^1\text{H}$ -MRS methodology. The robust signal change is visually discernible on individual  
 313 subject spectra (Fig.2)

Metabolite	Posterior cingulum						Whole gray matter						Whole white matter					
	conc.		CV	$\Delta\text{conc.}$		p	conc.		CV	$\Delta\text{conc.}$		p	conc.		CV	$\Delta\text{conc.}$		p
	(mean $\pm$ SD) (/tCr)	(mean $\pm$ SD) (%)	(%)	(mean $\pm$ SD) (%)	p-value		(mean $\pm$ SD) (/tCr)	(mean $\pm$ SD) (%)	(%)	(mean $\pm$ SD) (%)	p		(mean $\pm$ SD) (/tCr)	(mean $\pm$ SD) (%)	(%)	(mean $\pm$ SD) (%)	p	
Asp	1.93 $\pm$ 0.21	8.5 $\pm$ 3.9	15.0 $\pm$ 9.3	0.0221	8.5 $\pm$ 10.9	0.17	0.44 $\pm$ 0.02	6.2 $\pm$ 8.0	-5.9 $\pm$ 6.4	0.107	-3.4 $\pm$ 1.8	0.01	0.47 $\pm$ 0.03	3.9 $\pm$ 2.4	1.6 $\pm$ 1.5	0.0848	-2.3 $\pm$ 4.7	0.36
Cr	3.78 $\pm$ 0.12	2.0 $\pm$ 0.8	-1.6 $\pm$ 2.8	0.2563	-3.6 $\pm$ 3.6	0.09	-	-	-	-	-	-	-	-	-	-	-	-
Glc	1.46 $\pm$ 0.16	17.3 $\pm$ 7.1	9.5 $\pm$ 23.4	0.4472	9.0 $\pm$ 23.6	0.36	-	-	-	-	-	-	-	-	-	-	-	-
GPC	0.79 $\pm$ 0.08	4.0 $\pm$ 1.0	4.2 $\pm$ 4.0	0.0932	-4.5 $\pm$ 3.2	0.04	-	-	-	-	-	-	-	-	-	-	-	-
GSH	0.93 $\pm$ 0.05	5.8 $\pm$ 2.2	12.2 $\pm$ 11.2	0.0894	-0.3 $\pm$ 9.0	0.98	-	-	-	-	-	-	-	-	-	-	-	-
myo-Ins	5.28 $\pm$ 0.29	0.8 $\pm$ 0.1	-1.8 $\pm$ 0.9	0.0081	-0.6 $\pm$ 0.8	0.15	0.82 $\pm$ 0.05	2.3 $\pm$ 0.9	-0.1 $\pm$ 2.7	0.931	-0.6 $\pm$ 2.7	0.65	0.84 $\pm$ 0.07	2.2 $\pm$ 0.6	-0.4 $\pm$ 2.6	0.7662	-0.7 $\pm$ 3.8	0.74
slns	0.10 $\pm$ 0.05	11.8 $\pm$ 4.7	6.8 $\pm$ 11.6	0.3219	-0.9 $\pm$ 23.6	0.50	-	-	-	-	-	-	-	-	-	-	-	-
Lac	0.54 $\pm$ 0.29	22.3 $\pm$ 18.6	6.5 $\pm$ 21.9	0.8077	-102.6 $\pm$ 238.	0.63	-	-	-	-	-	-	-	-	-	-	-	-
PCr	2.60 $\pm$ 0.09	2.6 $\pm$ 0.9	0.3 $\pm$ 2.7	0.7468	2.2 $\pm$ 3.4	0.20	-	-	-	-	-	-	-	-	-	-	-	-
PCho	0.30 $\pm$ 0.03	10.3 $\pm$ 2.1	-11.7 $\pm$ 13.7	0.1103	6.1 $\pm$ 13.40	0.34	-	-	-	-	-	-	-	-	-	-	-	-
PE	2.37 $\pm$ 0.19	3.7 $\pm$ 1.1	1.7 $\pm$ 6.0	0.5823	-1.0 $\pm$ 5.6	0.72	-	-	-	-	-	-	-	-	-	-	-	-
NAA	9.50 $\pm$ 0.38	1.0 $\pm$ 0.3	-2.2 $\pm$ 1.6	0.0417	-0.4 $\pm$ 0.3	0.03	-	-	-	-	-	-	-	-	-	-	-	-
NAAG	0.64 $\pm$ 0.10	8.2 $\pm$ 3.8	0.0 $\pm$ 6.3	0.8999	2.1 $\pm$ 6.7	0.58	-	-	-	-	-	-	-	-	-	-	-	-
Tau	1.07 $\pm$ 0.15	4.9 $\pm$ 0.5	-9.6 $\pm$ 8.0	0.0641	6.4 $\pm$ 4.2	0.03	0.35 $\pm$ 0.02	4.2 $\pm$ 1.2	-5.9 $\pm$ 5.6	0.077	-1.2 $\pm$ 6.2	0.69	0.38 $\pm$ 0.03	3.6 $\pm$ 1.5	-3.4 $\pm$ 9.7	0.4758	-3.0 $\pm$ 7.2	0.39
Glu23	13.15 $\pm$ 0.27	1.9 $\pm$ 0.7	-2.9 $\pm$ 3.7	0.1546	0.4 $\pm$ 1.9	0.62	0.72 $\pm$ 0.04	2.3 $\pm$ 2.6	-5.1 $\pm$ 2.6	0.012	-4.2 $\pm$ 6.7	0.23	0.71 $\pm$ 0.02	2.7 $\pm$ 2.7	-5.1 $\pm$ 2.3	0.0068	-3.9 $\pm$ 6.8	0.28
Glu4	7.79 $\pm$ 0.25	1.3 $\pm$ 0.1	14.4 $\pm$ 2.3	<b>0.0001*</b>	-0.7 $\pm$ 2.3	0.55	0.54 $\pm$ 0.04	1.7 $\pm$ 1.8	13.4 $\pm$ 3.5	<b>0.001*</b>	-0.7 $\pm$ 1.3	0.35	0.50 $\pm$ 0.03	1.6 $\pm$ 1.5	14.0 $\pm$ 2.9	<b>0.0007*</b>	-2.4 $\pm$ 3.8	0.24
Gln23	0.64 $\pm$ 0.55	33.7 $\pm$ 14.1	11.3 $\pm$ 64.0	0.9393	-24.8 $\pm$ 56.1	0.26	-	-	-	-	-	-	-	-	-	-	-	-
Gln	-	-	-	-	-	-	0.30 $\pm$ 0.03	6.3 $\pm$ 4.1	-4.8 $\pm$ 7.9	0.288	-3.1 $\pm$ 8.5	0.46	0.30 $\pm$ 0.02	5.5 $\pm$ 3.1	0.3 $\pm$ 6.2	0.8439	-9.4 $\pm$ 8.8	0.07
Gln4	2.84 $\pm$ 0.35	4.3 $\pm$ 1.6	12.3 $\pm$ 4.5	<b>0.0019*</b>	1.9 $\pm$ 5.0	0.35	-	-	-	-	-	-	-	-	-	-	-	-
GABA	-	-	-	-	-	-	0.23 $\pm$ 0.02	2.9 $\pm$ 1.7	-3.0 $\pm$ 4.4	0.215	-5.1 $\pm$ 7.4	0.20	0.23 $\pm$ 0.01	2.8 $\pm$ 1.1	-2.2 $\pm$ 4.8	0.3675	-3.9 $\pm$ 7.1	0.26
GABA2	1.22 $\pm$ 0.24	8.2 $\pm$ 1.2	8.8 $\pm$ 19.5	0.2376	-3.8 $\pm$ 15.1	0.58	-	-	-	-	-	-	-	-	-	-	-	-
GABA34	1.82 $\pm$ 0.65	20.0 $\pm$ 14.4	-6.8 $\pm$ 21.2	0.7203	-8.7 $\pm$ 42.2	0.89	-	-	-	-	-	-	-	-	-	-	-	-
Glc+Tau	2.53 $\pm$ 0.26	1.5 $\pm$ 0.6	0.8 $\pm$ 14.9	0.9512	7.8 $\pm$ 15.4	0.25	-	-	-	-	-	-	-	-	-	-	-	-
tCh	1.08 $\pm$ 0.08	1.1 $\pm$ 0.4	0.9 $\pm$ 3.4	0.5877	-1.4 $\pm$ 3.0	0.37	0.33 $\pm$ 0.02	0.9 $\pm$ 0.8	-2.3 $\pm$ 1.8	0.050	-0.5 $\pm$ 1.9	0.60	0.35 $\pm$ 0.23	1.0 $\pm$ 0.6	-1.7 $\pm$ 1.8	0.1051	-0.9 $\pm$ 2.1	0.43
tCr	6.38 $\pm$ 0.11	1.2 $\pm$ 0.5	-0.8 $\pm$ 1.7	0.3335	-1.2 $\pm$ 1.8	0.22	1.00 $\pm$ 0.00	-	-	-	-	-	1.00 $\pm$ 0.00	-	-	-	-	-
tNAA	10.14 $\pm$ 0.45	1.9 $\pm$ 0.3	-2.1 $\pm$ 1.6	0.0481	-0.3 $\pm$ 0.5	0.23	1.47 $\pm$ 0.08	1.9 $\pm$ 2.5	1.1 $\pm$ 3.9	0.575	-1.2 $\pm$ 2.2	0.30	1.59 $\pm$ 0.06	1.7 $\pm$ 2.2	1.4 $\pm$ 3.2	0.4114	-0.3 $\pm$ 2.1	0.78

**Table 1.** Metabolite concentration estimates, stability, and temporal changes with and without deuterated glucose. Data are calculated from concentrations quantified in  $\mu\text{mol/g}$  for single-voxel MRS and referenced to total creatine (tCr) for 3D-MRSI. The regional means from the gray and white matter voxels were used to calculate between-subject averages in metabolite concentrations. The average concentrations and their respective coefficients of variations measured immediately after nonDeu-Glc administration (the first time-point). The within-session differences were calculated by subtracting the concentrations of the first and last data point, and their statistical significance was assessed via a standard, two-tailed, paired t-test (separately for Deu and nonDeu scans). The asterisks indicate statistical significance after correction for multiple comparisons with the false discovery rate method, which limited the likelihood of false positives to 3%.

314

315

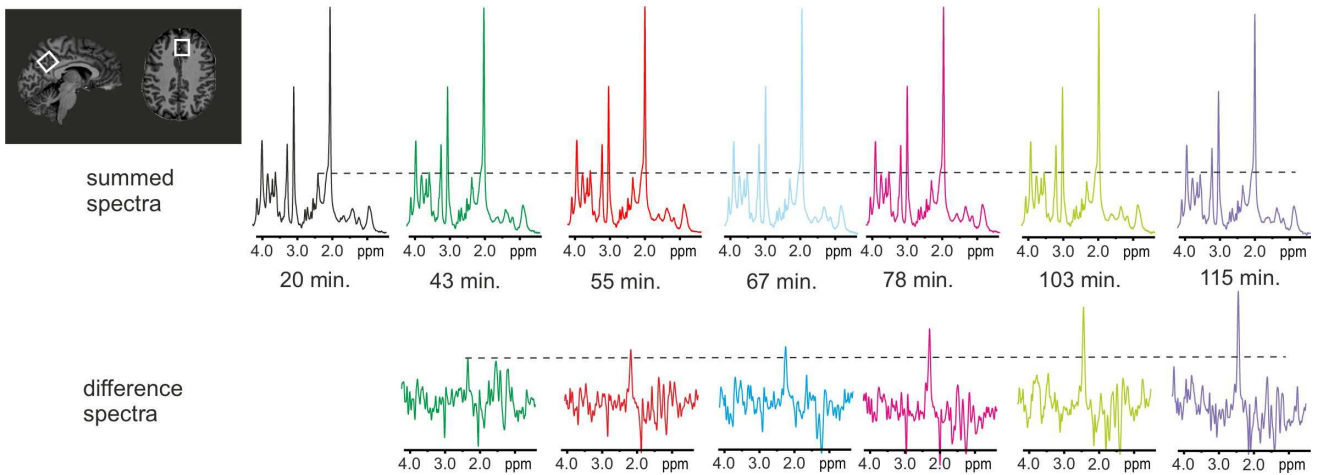


**Fig. 2. Example of single-voxel MR spectra obtained in the posterior cingulum in one participant.** The displayed spectra were obtained after peroral administration of Deu-Glc. The summed spectra in the upper row show decreasing signal at the resonance frequency of  $-C4^1H_2-$  in the glutamate molecule (2.34 ppm) due to enrichment of the glutamate pool with  $^2H$  (either  $-C4^2H^2H-$  or  $-C4^2H^1H-$ ). The robust change at the 4<sup>th</sup> carbon position is documented by the increasing signal amplitude at 2.34 ppm in the difference spectra calculated by subtraction of the respective spectrum from the last session minus the first session.

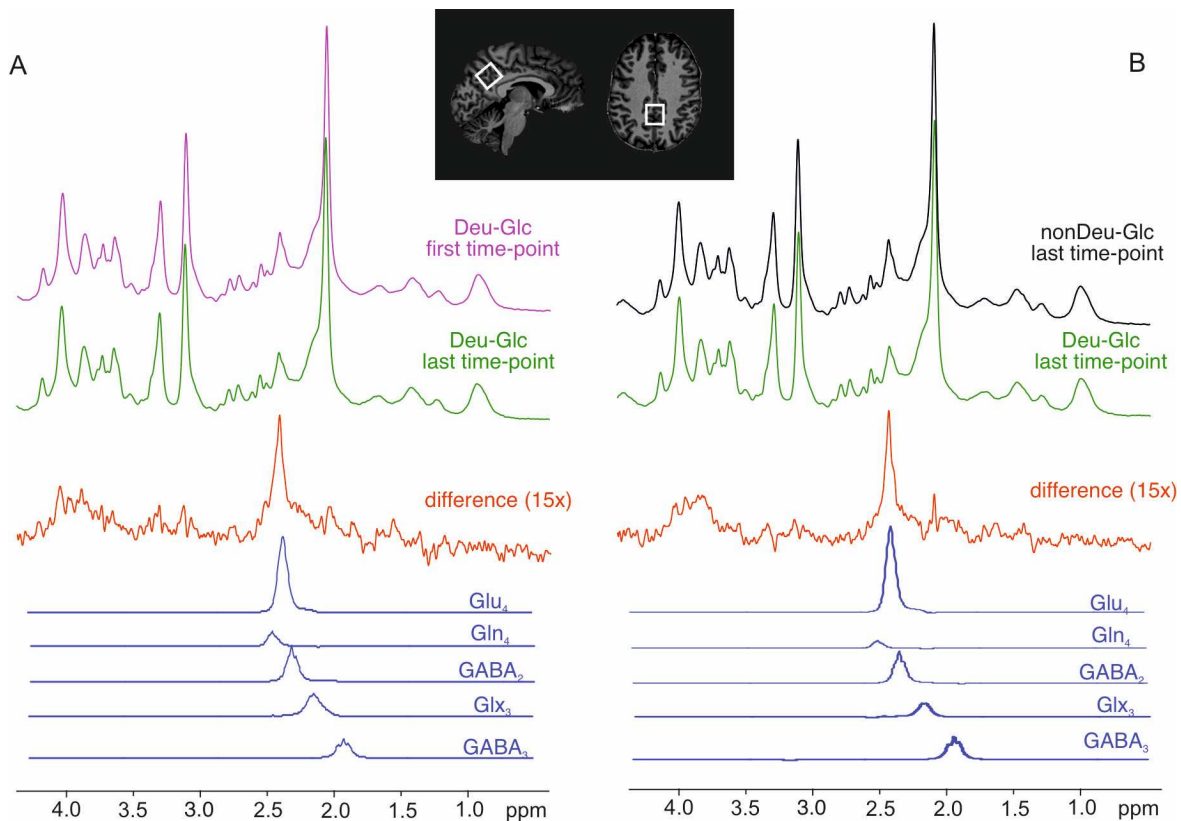
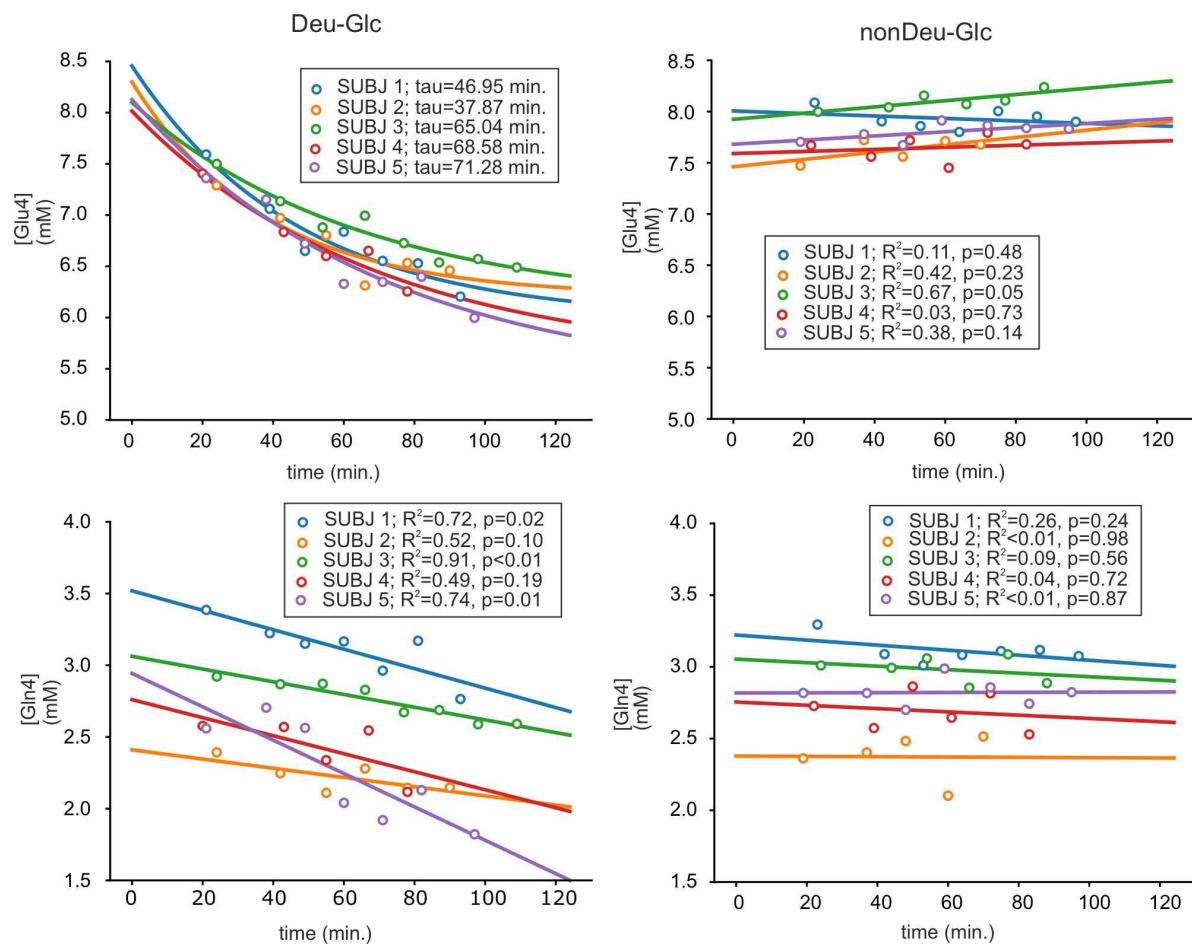


**Fig.3. Difference spectra and their quantification.** Summed spectra from all subjects (N=5) represent the first and last time-points after Deu-Glc and nonDeu-Glc ingestion. The spectra in panel A and B were linewidth-matched with exponential line-broadening and subtracted. While the resulting difference spectrum in panel A represents the effect of metabolite Deu enrichment, the similar difference spectrum in panel B corroborates the fact that metabolite changes were not related to the nonDeu-Glc administration, but were, indeed, a consequence of the deuterium enrichment. The difference spectra reflect oscillations of the Glc signal after Deu/nonDeu-Glc administration. The metabolite components were obtained via LCModel analysis using a basis set containing simulated spectra of neurochemicals that were undergoing deuteration (i.e., Glu, Gln, and GABA). The proton signals that originated from different carbon groups were separated.

317 To corroborate the LCModel analysis of single-subject data, high-SNR spectra were  
 318 calculated by summing the spectra from all subjects (N = 5). The summed spectra and their  
 319 differences displayed in Fig. 3 clearly demonstrate the effect of deuterium enrichment (Fig.  
 320 3A) and rule out hyperglycemia and/or acquisition instabilities as possible confounders (Fig,  
 321 3B). While the quantification of single-subject time-courses did not reveal a change in GABA<sub>2</sub>,  
 322 the quantification of difference spectra yielded Cramér-Rao lower bounds, i.e., the estimates  
 323 of quantification error, of 16% for GABA<sub>2</sub>.

324

325 While the exponential and linear fits of Glu<sub>4</sub> and Gln<sub>4</sub> data clearly demonstrated decaying  
 326 signals in the Deu-Glc session, the linear fitting of the paired nonDeu-Glc data showed stable  
 327 Glu<sub>4</sub> and Gln<sub>4</sub> concentrations during the session (Fig. 4). The exponential rate constants (tau)  
 328 were obtained per subject from Glu<sub>4</sub> with a coefficient of variation of 26%. The decaying  
 329 slopes of Gln<sub>4</sub> were obtained with a between-subject variance of 50%.



330 **Fig. 4. Fitting of time courses obtained by quantification of single-voxel MR spectra in LCModel.**  
 331 Decay in the concentrations of glutamate (Glu<sub>4</sub>) and glutamine (Gln<sub>4</sub>) were fitted using the exponential  
 function  $Y=Y_0^{-t/\tau}+c$  (Glu<sub>4</sub>), and linear regression  $Y = a + bX$  (Gln<sub>4</sub>). The time-courses and their fits  
 following Deu-Glc ingestion contrast with those with stable Glu<sub>4</sub> and Gln<sub>4</sub> fits in nonDeu-Glc sessions.  
 Overall, concentrations of 14 metabolites were quantified with average within-session CVs  
 below 5% (MM, Cr, GPC, myo-Ins, PCr, PE, NAA, Tau, Glu<sub>2+3</sub>, Glu<sub>4</sub>, Gln<sub>4</sub>, tCho, tCr, tNAA),

332 and another eight (Asp, Glc, GSH, scyllo-Ins, PCh, NAAG, GABA<sub>2</sub>, Glc+Tau) with CVs below  
333 20% as assessed from concentrations obtained from the nonDeu-Glc scan (Table 1).

334

335

### 336 **3D-MRSI: voxel-wise time-course analysis**

337

338 Analysis of time-courses on a per-voxel basis revealed a drop in Glu signal at the C4 position  
339 (Glu<sub>4</sub>) by 13.4%±3.5% in GM (p = 0.001) and 14.0%±2.9% in WM (p = 0.0007, Table 1). For  
340 all other reliably quantified metabolites, no significant changes were found during the Deu-  
341 Glc scan (Table 1). As expected, all metabolites were stable during the nonDeu-Glc session  
342 (tCho, tNAA, GABA, Gln, Glu<sub>4</sub>, Glu<sub>2+3</sub>, myo-Ins). The regional difference in the Glu<sub>4</sub> drop  
343 between GM and WM during the Deu-Glc session was reflected by the spectra shown in Fig.  
344 5. The signal attenuation around 2.34 ppm (i.e., Glu<sub>4</sub> resonance) and no other major signal  
345 changes in other LCModel-quantified spectral regions (1.9-4.2 ppm) corroborated the robust  
346 detection of ΔGlu<sub>4</sub> with single-subject spectral analysis during the Deu-Glc experiment.

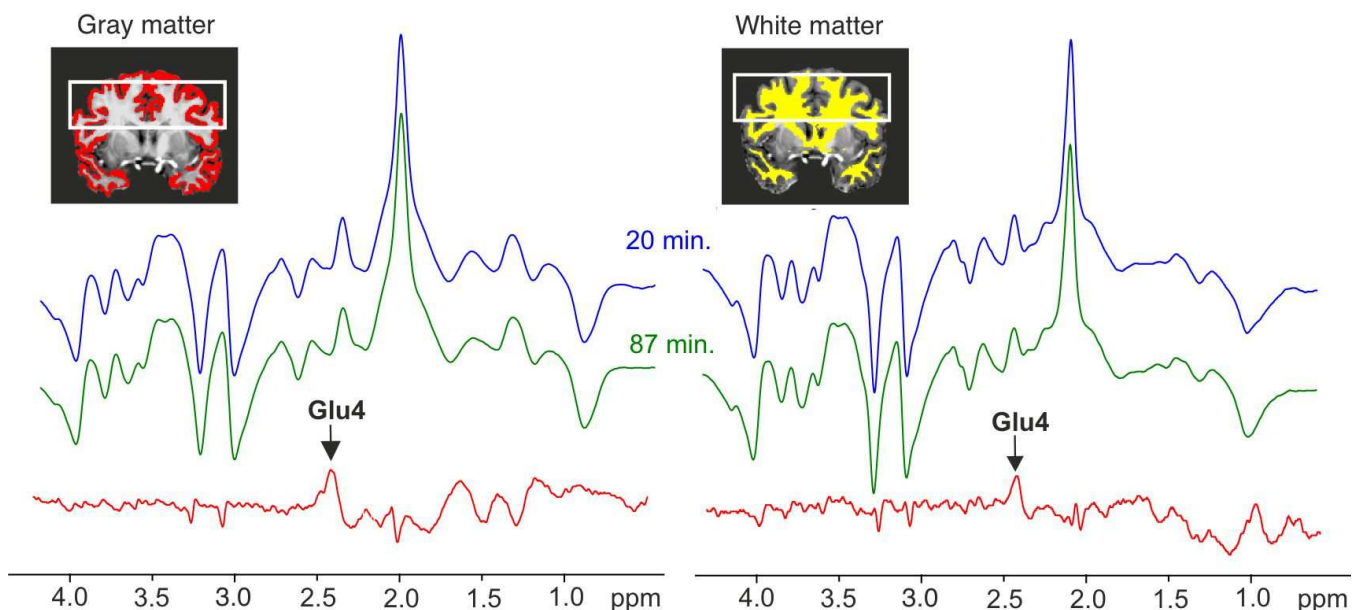
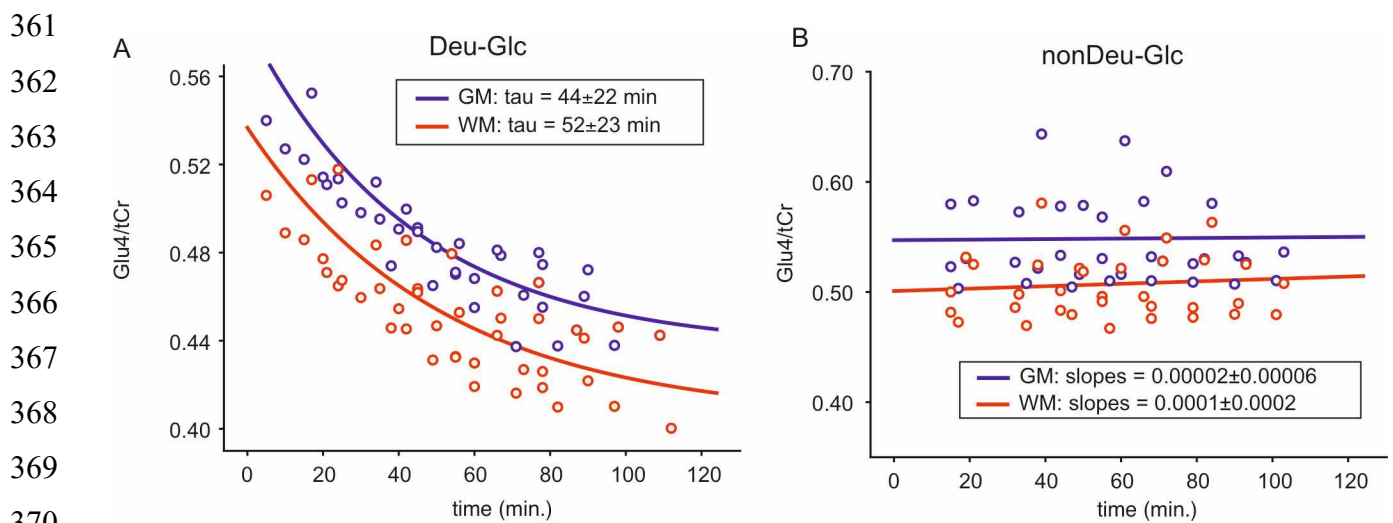


**Fig 5. Effect of Deu-Glc on the spectra obtained from the gray and white matter with 3D multivoxel MRS.** Difference spectra were calculated by subtraction of spectra obtained from the first and last time-point after deuterium ingestion in one healthy volunteer. The spectra were selected using a quality control mask and segmented gray or white matter masks. The signal loss at 2.34 ppm reflects the exchange of protons and deuterons at the 4<sup>th</sup> carbon position in the glutamate molecule and is displayed as a positive peak in the difference spectra. The signal decay is convincingly found in both gray and white matter. Lack of unwanted signals in the quantified range 1.9-4.2 ppm verifies good spectral quality and stability during the acquisition.

347

348 As the magnitude of Glu<sub>4</sub> signal attenuation is influenced by the variable initiation and  
349 duration of the MRS data acquisition among scans, each single-subject temporal MRSI  
350 dataset was fitted with an exponential function to characterize the speed of signal decay—

351 the time constant ( $\tau$ )—which is well characterized in each scan session. The averaged fits  
 352 are shown in Fig.6. The exponential fit of  $\text{Glu}_4$  concentrations yielded  $\tau$  values (the rate  
 353 constants) of  $44 \pm 22$  minutes and  $52 \pm 23$  minutes in GM and WM, respectively, in the Deu-Glc  
 354 sessions. The decay was 18% faster in GM than in WM, on average. The linear regression  
 355 of the  $\text{Glu}_4/\text{tCr}$  time-courses measured during the nonDeu-Glc session (exponential fits)  
 356 yielded non-significant slopes of  $0.00002 \pm 0.00006$  and  $0.0001 \pm 0.0002$  ( $p > 0.07$ ), thus  
 357 indicating no effect of glucose load on the  $\text{Glu}_4$  and good stability of the measurements. While  
 358 the between-subject CVs for the concentration differences in  $\text{Glu}_4$  were 26% (GM) and 21%  
 359 (WM), the respective CVs calculated from the rate constants ( $\tau$ ) were 50% (GM) and 45%  
 360 (WM).



361 **Fig 6. Fitting of time courses from averaged regional MRSI maps:** Exponential averaged decays  
 362 of  $\text{Glu}_4/\text{tCr}$  within-session time-courses after Deu-Glc ingestion (A) are in contrast with stable linear  
 363 fits for  $\text{Glu}_4/\text{tCr}$  after nonDeu-Glc (B). The exponential fits showed 18% faster decay (smaller  
 364 constant of the decay –  $\tau$ ,  $M = M_0 e^{-t/\tau} + c$ ) in the gray (blue) than in the white matter (red).  
 365  
 366  
 367  
 368  
 369  
 370

371 In GM and WM,  $372 \pm 169$  and  $737 \pm 280$  voxels, respectively, fulfilled the quality assessment  
 372 criteria and were, thus, used to calculate regional means for each time-point and their CVs  
 373 per session (Table 1). LCModel quantified 10 metabolites referenced to tCr with within-  
 374 session CVs below 7%, i.e., Asp, myo-Ins, Tau,  $\text{Glu}_{2+3}$ ,  $\text{Glu}_4$ , Gln, GABA, tCho, and tNAA as  
 375 assessed on the data measured in the nonDeu-Glc session. Namely,  $\text{Glu}_4$  was consistently  
 376 quantified with CVs below 2% in both GM and WM.  
 377  
 378  
 379  
 380

381 Finally, single-subject MRSI time-courses obtained with high time resolution (Fig. 7A, 7B)  
 382 were fitted with linear regression per voxel (Fig. 7C). The resulting slopes ( $p < 0.05$ ,  $r < -0.8$ )  
 383 were steeper in the GM than in the WM by 19% and yielded a contrast between gray and  
 384 white matter on the slope map (Fig. 7C). The linear regression was found more appropriate

385 than using an exponential function to fit time-courses obtained from each voxel with a lower  
 386 signal-to-noise ratio than time-courses that used regional means, as shown in Fig. 7B.

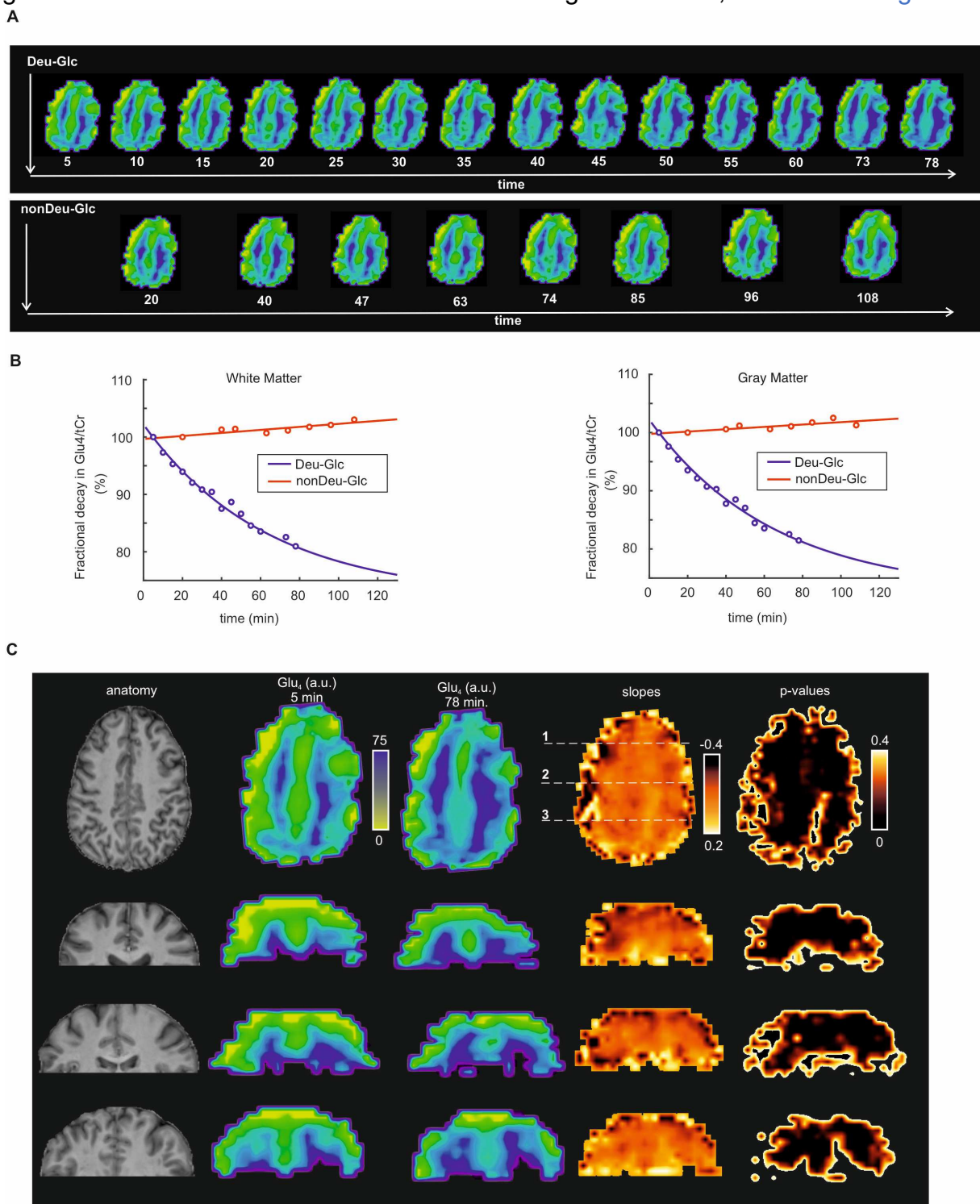


**Fig 7. Voxel-wise fitting of glutamate time-courses obtained with high time resolution.** MRSI data were acquired in one participant with a time-resolution of five minutes after peroral administration of Deu-Glc (panel A). Spectral postprocessing included channel-wise L2-regularization for suppression of unwanted lipid signals. Maps demonstrate the signal decay of protons on the 4<sup>th</sup> carbon position in the glutamate molecule (Glu<sub>4</sub>). The stable Glu<sub>4</sub> from the session after the ingestion of nonDeu-Glc are displayed for comparison. The plots (panel B) show fractional decay of regional Glu<sub>4</sub> averages in the gray and white matter regions. Voxel-wise linear regression was applied to Glu<sub>4</sub> time-courses (panel C). Respective slopes tend to be higher in the gray matter, which suggests a higher glutamate turnover in the gray than in the white matter.

387 **Discussion (2008 words)**

388

389 The current work reveals the tremendous potential of deuterium labeling to measure the  
390 turnover of metabolites involved in oxidative glucose metabolism in the human brain.  
391 Impaired glucose homeostasis and mitochondrial dysfunction are key components in the  
392 pathophysiology of neurodegenerative diseases, such as Alzheimer's and other forms of  
393 dementia, and also in metabolic disorders, including obesity and insulin resistance,<sup>32</sup> moving  
394 the imaging of brain glucose metabolism to center stage.<sup>33</sup> The development of non-invasive  
395 methods that enable objective, dynamic, and longitudinal metabolic tracking in health,  
396 disease, and aging are urgently needed to track the treatment effects and support emerging  
397 therapies.<sup>34</sup>

398

399 Here, we established for the first time dynamic downstream Glu mapping after Deu-Glc  
400 administration using a novel multi-voxel <sup>1</sup>H-MRSI sequence, which was corroborated by the  
401 well-established, single-voxel, functional MRS methodology.<sup>12,28</sup> Our work benefited from the  
402 combination of ultra-high-field (7T) and a high natural abundance of protons in the human  
403 body. Our indirect detection of <sup>2</sup>H with <sup>1</sup>H-MRS(I) utilized commercially available  
404 radiofrequency coils and optimized <sup>1</sup>H-MRS approaches to overcome the major drawbacks  
405 of direct techniques tuned to the deuterium frequency (<sup>2</sup>H-MRS) that require dedicated coils  
406 and pulse sequences.<sup>35</sup> Compared to <sup>2</sup>H-MRS, our proposed indirect approach also enabled  
407 the detection of GABA changes and the separation of Glu from Gln, which is not feasible  
408 using <sup>2</sup>H-MRS even at ultra-high MR fields (16.4T) due to the limited spectral resolution of  
409 <sup>2</sup>H-spectra.<sup>36</sup> The orally administered deuterated Glc is safe, stable, and affordable compared  
410 to radioactive PET tracers with short half-lives, which require technically challenging onsite  
411 preparation and expensive cyclotrons. We have also demonstrated the potential of <sup>2</sup>H-to-<sup>1</sup>H-  
412 MRS to overcome the challenges of <sup>13</sup>C-MRS, which was previously the only method for  
413 quantitative assessment of TCA kinetics and Glu and Gln cycling. We demonstrated that  
414 modified basis sets with separated Glu and Gln components on the C4 position enabled the  
415 extraction of quantitative information about Glu and Gln turnover in a manner similar to that  
416 of the technically challenging <sup>13</sup>C-MRS. Although we could not convincingly track GABA  
417 changes in individual data, our results demonstrated signal changes in GABA<sub>2</sub> on the group  
418 level using difference spectra calculated from pooled data with reasonable quantification  
419 errors (CRLB of 16%). The analysis of difference spectra convincingly corroborated Gln<sub>4</sub> and  
420 Glu<sub>4</sub> changes captured in individual data. The fitting of difference spectra constructed by  
421 subtracting spectra pooled from multiple subjects indeed benefits from a high signal-to-noise

422 ratio and elimination of signals from static metabolites, including the molecular background.  
423 We expect a further boost of quantification of J-coupled relatively low-abundant metabolites  
424 such as GABA and Gln by optimization of the sequences for higher fields (i.e., above 7T)  
425 and/or by spectral editing techniques, possibly enabling robust GABA detection even at low-  
426 field MR scanners.<sup>37,38</sup>

427

428 The fact that the resting and the stimuli-activated brain both utilize the same mitochondrial  
429 oxidative pathway highlights the incredible clinical utility of deuterium imaging. Deuterium  
430 imaging might thus measure Glu, Lac, Asp, and Glc modulations after neuronal activation in  
431 response to visual stimulation or various pharmacological interventions.<sup>18,39</sup> The deuteration  
432 of molecules (i.e., replacing  $^1\text{H}$  with  $^2\text{H}$  nuclei) is a simple chemical procedure that allows  
433 labeling of a broad range of substances with minimal influence on their *in vivo* kinetics within  
434 metabolite cycles.<sup>40</sup> Other deuterated tracers, such as deuterated choline, could be detected  
435 indirectly with  $^1\text{H}$ -MRS, and its increased uptake has been shown in brain tumors with direct  
436  $^2\text{H}$ -MRS.<sup>41</sup> Deuterium metabolic imaging will also allow the utilization of deuterated-ketone  
437 bodies, such as beta-hydroxybutyrate (BHB)<sup>42</sup> and acetate,<sup>8</sup> which serve as alternative brain  
438 fuels, especially during fasting, with critical implications in AD,<sup>44</sup> some forms of epilepsy<sup>45</sup>,  
439 and brain tumors. While we did not detect any lactate changes due to minimal employment  
440 of the glycolytic paths in the healthy brain,  $^1\text{H}$ -MRS is highly sensitive to lactate.<sup>12</sup> Indirect  $^2\text{H}$ -  
441 to- $^1\text{H}$ -MRS(I) can be thus used to measure the Warburg effect, a shift toward anaerobic  
442 glycolysis due to mitochondrial failure in ischemia and brain tumors, as shown in animal  
443 glioma models.<sup>1</sup> Increased lactate is also a hallmark of aging-related mitochondrial  
444 dysfunction,<sup>46</sup> and it is conceivable that lactate production accompanies deteriorated Glu  
445 production via the TCA cycle in neurodegeneration.<sup>47</sup> Thus, the characterization of the main  
446 Glc pathways through Lac and Glu dynamics extends the clinical utility of this method.

447

448 Our study demonstrated major methodical advancements that are critical for future  
449 applications. We reduced the voxel volume, minimized the partial volume effect, and  
450 achieved substantial signal gain due to the implementation of a concentric ring trajectory  
451 readout.<sup>11,25</sup> We have already demonstrated that MRSI can be further accelerated via k-  
452 space undersampling to extend the coverage of  $^2\text{H}$ -to- $^1\text{H}$ -MRSI over the whole brain.<sup>23</sup> The  
453 spatial resolution in our project was almost two magnitudes higher than for previous direct  
454  $^2\text{H}$ -MRSI studies at 4T (0.12 mL vs. 8 mL).<sup>35</sup>

455

456 The nearly twenty percent difference in the glutamate turnover in the gray and white matter  
457 is in line with the current gold standard ( $[^{18}\text{F}]\text{FDG}$ -PET studies, which measured the  
458 differences in the CMRGlc (oxidative) at 0.18 and 0.24  $\mu\text{mol/g/min}$ ,<sup>48,49</sup> i.e., ~33% higher  
459 oxidative Glc consumption ascribed to the higher inhibitory and excitatory demands of the  
460 gray matter.<sup>50</sup> However, the between-subject differences (last minus first point) in Glu<sub>4</sub> were  
461 more similar in the PCC ( $\Delta\text{Glu}_4=14\%$ , 80% GM/WM fraction, SV-MRS) than in the GM  
462 ( $\Delta\text{Glu}_4=13\%$ , MRSI) and WM ( $\Delta\text{Glu}_4=14\%$ , MRSI). This indicates that similar relative  
463 differences between the first point and steady-state are achieved at a different speed. The  
464 robust detection of within-session differences in Glu<sub>4</sub> was enabled by excellent CVs (2% for  
465 both methods), which were well below the detected differences. While the between-subject  
466 variance in the concentration differences between the first point and the last point was 19%  
467 (PCC - SV-MRS), 26% (GM - MRSI), and 21% (WM – MRSI), the between-subject variance  
468 in Glu rates appeared similar for MRS (~ 25%) and higher for MRSI (50% for GM and 45%  
469 for WM). Thus, MRS fitting yielded a similar variance from the gold standard ( $[^{18}\text{F}]\text{FDG}$ -PET  
470 measures of CMRGlc, reported in the range of 19%-29% (mean – median) between  
471 subjects.<sup>51,52</sup> This can be mainly ascribed to high physiological variation in the resting brain  
472 metabolism. Also, this is a preliminary study, and further technical improvements are  
473 expected to yield even higher reproducibility also on a voxel-by-voxel level. The variance can  
474 be further lowered by using only a single, e.g., only  $^2\text{H}$ -to- $^1\text{H}$ -MRSI technique, thereby  
475 improving the time resolution and the exponential fits (Fig 7B) and yielding ~3x more time  
476 points than the current study. The stability of the measurements might be further increased  
477 by prospective motion correction methods based on tracking with an optical camera or  
478 navigators,<sup>53</sup> further boosting the stability of quantification while refining the assessment of  
479 smaller brain regions. The drawbacks of the current  $^1\text{H}$ -MRSI methods can be overcome by  
480 advanced  $B_0$  shimming approaches, such as higher-order shims above 2<sup>nd</sup> order,  
481 complementary matrix  $B_0$  shims, and dynamic shim updates to mitigate temporal  $B_0$   
482 instabilities during dynamic acquisitions. These advancements will make challenging brain  
483 regions (hippocampus) and more spectral components accessible with higher reproducibility.  
484 Finally, a major developmental aspect will be the incorporation of (k,t)-undersampling  
485 methods, which are routinely used in clinical, dynamic, contrast-enhanced MRI<sup>54</sup> and for  
486 which >10-fold improvements in temporal resolution or alternatively higher spatial resolution  
487 at similar temporal resolution are currently commonly achieved without compromising spatial  
488 resolution.<sup>55,56</sup> Despite these methodological limitations, we clearly proved that observed  
489 metabolite changes are related to deuterium enrichment and the measured signal time  
490 courses are suitable for quantitative modeling of metabolite kinetics. The two-session design

491 demonstrated that metabolite changes were not related to instability in the spectral quality or  
492 the metabolic effects of hyperglycemia.

493

494 While the minimally invasive peroral administration of the tracer highlights the clinical utility  
495 of our approach, it might limit the interpretation of brain Glc levels. Glc time-courses during  
496 the acquisition reflects the plasmatic concentrations during the experiment, which resembles  
497 the oral Glc tolerance test and prolonged resorption of the glucose from the stomach. The  
498 Glc concentration measured in the brain is a mix of Glc signals originating from the vascular  
499 and brain tissue compartments and would not allow neglecting vascular Glc concentrations  
500 during prolonged hyperglycemia.<sup>36</sup> Thus, the interpretation of Glc time-courses is not entirely  
501 straightforward. However, the sensitive detection of Glc differences between non-Deu-Glc  
502 and Deu-Glc sessions (~0.3 mM) and excellent quantification accuracy ( $CRLB_{Glc+Tau} = \sim 7\%$ )  
503 with SV-MRS promise feasible tracking of Glc increase after incorporation of Deu-Glc to  
504 downstream metabolism. Future studies will benefit from blood sampling to measure blood  
505 glucose deuterium enrichment as a function of time or intravenous Deu-Glc administration  
506 and quantitative compartmental modeling approaches.<sup>57</sup> Indeed, in the intravenous  
507 experiment, the blood Deu-Glc enrichment dropped shortly after the bolus of the tracer and  
508 could be neglected in the metabolite modeling.<sup>36</sup> The peroral Deu-Glc load and postprandial  
509 hyperglycemia can complicate the clinical scenarios when glucose homeostasis is  
510 compromised, for example, in diabetic patients.

511

512 The primary hormone responsible for the regulation of peripheral and brain glucose  
513 metabolism is insulin, which is released from the endocrine pancreas in response to rising  
514 blood glucose levels. Insulin is transported across the blood-brain barrier to the CNS via  
515 saturable transporters, affecting both brain function and peripheral metabolism.<sup>14</sup> While  
516 peripheral hyperinsulinemia does, indeed, lead to brain hyperinsulinemia, their extent and  
517 kinetics are distinct since the transport of insulin to the brain is saturable, and the insulin has  
518 a longer half-life in the brain than in the periphery<sup>58</sup>. There is no clear consensus about  
519 whether and how systemic hyperinsulinemia affects brain metabolism.<sup>59–61</sup> Although we did  
520 not observe significant changes in metabolite levels after dextrose administration, in  
521 agreement with the previous study,<sup>62</sup> we cannot rule out that hyperglycemia and  
522 hyperinsulinemia affect the speed of deuterium enrichment that is not accompanied by  
523 changes in metabolite concentrations. In another study, however, insulin infusion did not  
524 significantly impact glucose transport kinetics with plasma insulin concentrations up to 100  
525 pmol/L.<sup>60</sup> Therefore, our measurements of metabolite decays with postprandial (moderate)

526 plasma insulin levels are unlikely affected by insulin increase after tracer ingestion in subjects  
527 without insulin intolerance. Also, in another study, the circulating insulin did not influence the  
528 brain glucose uptake, but the insulin resistance status significantly affected brain glucose  
529 kinetics.<sup>63</sup> Hence, while peripheral insulin does not play a significant role in the brain glucose  
530 metabolism, the metabolic effects of central insulin action and resistance could be more  
531 pronounced. Obesity and type 2 diabetes are associated with alterations in glucose  
532 metabolism and insulin resistance, including central insulin signaling defects,<sup>64</sup> which also  
533 play an essential role in AD development.<sup>65</sup> In addition, the transport of insulin across the  
534 blood-brain barrier is affected by insulin resistance and obesity.<sup>66</sup> Thus, applying the current  
535 methodology in the setting of pronounced insulin resistance might require the exclusion of  
536 differences in systemic insulin levels, which can be achieved by combination with a  
537 pancreatic clamp.

538

539 Due to recent advancements, it is plausible that the technique can be applied on widely  
540 available 3T clinical scanners.<sup>10,34</sup> Whereas 7T MR scanners have recently been clinically  
541 approved, they are still not as widely available as lower field 3T scanners. Indeed, 3T SV-  
542 MRS detected subtle Glu and Glc responses to visual stimulation on the order of 3-4% (Glu)  
543 and ~20% (Glc)<sup>67</sup> and similar <sup>1</sup>H-MRSI techniques for whole brain Glu mapping within 4  
544 minutes<sup>34</sup> promise implementation of the indirect Deu-MRS(I) despite the lower spectral and  
545 reduced spatial resolution at 3T.

546

547 Noninvasive quantification and imaging of metabolite changes relevant to the glucose  
548 metabolism and neurotransmitter synthesis (Glu/Gln, GABA) are beneficial for virtually all  
549 brain disorders. Here, we have introduced a novel, affordable approach for metabolic  
550 measures that utilizes widely available <sup>1</sup>H-MR scanner equipment to detect deuterated  
551 compounds indirectly and can thus be easily used in clinical applications. The negligible risk  
552 associated with deuterium administration compared to radioactive ([<sup>18</sup>F]FDG predetermines  
553 the methodology, especially for studies with a multi-session design to track treatment effects  
554 or disease progression over time. In contrast to direct <sup>2</sup>H-MRS, proton-MRS allows  
555 quantification of a vastly extended neurochemical profile, including non-deuterated  
556 compounds. Thus, the current methodology provides a critical step forward for future  
557 metabolic projects in the resting or activated brain in disease, health, and aging, which will  
558 offer relevant metabolic information using widely available hardware in a single MR session.

559

560 **Acknowledgments:** Authors thank Dr. Patrick Bolan, Center from Magnetic Resonance  
561 Research, University of Minnesota, and Dr. Chris Rogers, University of Cambridge, for  
562 providing a tool to store and apply 7T B<sub>0</sub>-shims at 7T MR scanner. The authors acknowledge  
563 helpful discussions with Dr. Vladimir Mlynarik. The authors are grateful to all study  
564 participants for volunteering in the study.

565

566 **Grant support/Funding:** PB was supported by the European Union's Horizon 2020 research  
567 and innovation program under a Marie Skłodowska-Curie grant agreement, no. 846793, and  
568 by a NARSAD Young Investigator Grant from the Brain and Behavior Research Foundation,  
569 no. 27238. AS has received funding from the European Union's Horizon 2020 research and  
570 innovation program under a Marie Skłodowska-Curie grant agreement, no. 794986. WB and  
571 GH acknowledge support by the Austrian Science Fund (FWF) grants P 30701, KLI 718  
572 (WB), and KLI 646 (GH), respectively. TS was supported by FWF grant KLI 782.

573

574 **Declaration of conflicting interests:**

575 R. Lanzenberger received travel grants and/or conference speaker honoraria within the last  
576 three years from Bruker BioSpin MR andHeel, and has served as a consultant for Ono  
577 Pharmaceutical. He received investigator-initiated research funding from Siemens  
578 Healthcare regarding clinical research using PET/MR. He is a shareholder of the start-up  
579 company BM Health GmbH since 2019.

580

581 The other authors declared no potential conflicts of interest with respect to the research,  
582 authorship, and/or publication of this article.

583

584 **Bibliography:**

585

- 586 1. Rich, L. J. *et al.* 1H magnetic resonance spectroscopy of 2H-to-1H exchange  
587 quantifies the dynamics of cellular metabolism in vivo. *Nat. Biomed. Eng.* **4**, 335–342  
588 (2020).
- 589 2. van Zijl, P. C. M. & Brindle, K. M. Spectroscopic measurements of metabolic fluxes.  
590 *Nat. Biomed. Eng.* **4**, 254–256 (2020).
- 591 3. Zhu, X.-H., Lu, M. & Chen, W. Quantitative imaging of brain energy metabolisms and  
592 neuroenergetics using in vivo X-nuclear 2H, 17O and 31P MRS at ultra-high field. *J.*  
593 *Magn. Reson.* **292**, 155–170 (2018).
- 594 4. Koppenol, W. H., Bounds, P. L. & Dang, C. V. Otto Warburg's contributions to current  
595 concepts of cancer metabolism. *Nature Reviews Cancer* (2011) doi:10.1038/nrc3038.

- 596 5. Norat, P. *et al.* Mitochondrial dysfunction in neurological disorders: Exploring  
597 mitochondrial transplantation. *npj Regenerative Medicine* (2020) doi:10.1038/s41536-  
598 020-00107-x.
- 599 6. Manji, H. *et al.* Impaired mitochondrial function in psychiatric disorders. *Nature*  
600 *Reviews Neuroscience* (2012) doi:10.1038/nrn3229.
- 601 7. Hesketh, R. L. *et al.* Magnetic Resonance Imaging Is More Sensitive Than PET for  
602 Detecting Treatment-Induced Cell Death–Dependent Changes in Glycolysis. *Cancer*  
603 *Res.* **79**, 3557–3569 (2019).
- 604 8. Rothman, D. L. *et al.* Methods | <sup>13</sup>C MRS Measurements of in Vivo Rates of the  
605 Glutamate/Glutamine and GABA/Glutamine Neurotransmitter Cycles. in *Encyclopedia*  
606 *of Biological Chemistry III* (2021). doi:10.1016/b978-0-12-819460-7.00341-8.
- 607 9. Wang, Z. J. *et al.* Hyperpolarized <sup>13</sup>C MRI: State of the art and future directions.  
608 *Radiology* (2019) doi:10.1148/radiol.2019182391.
- 609 10. Terpstra, M. *et al.* Test-retest reproducibility of neurochemical profiles with short-  
610 echo, single-voxel MR spectroscopy at 3T and 7T. *Magn Reson Med* **76**, 1083–1091  
611 (2016).
- 612 11. Hingerl, L. *et al.* Clinical High-Resolution 3D-MR Spectroscopic Imaging of the  
613 Human Brain at 7 T. *Invest. Radiol.* **55**, 239–248 (2020).
- 614 12. Bednarik, P. *et al.* Neurochemical and BOLD responses during neuronal activation  
615 measured in the human visual cortex at 7 Tesla. *J Cereb Blood Flow Metab* **35**, 601–  
616 610 (2015).
- 617 13. Bednarik, P. *et al.* Functional spectroscopic imaging (fMRSI) detects metabolite  
618 changes in the activated primary sensorimotor cortex at 7T. in *Meeting of the*  
619 *International Society for Magnetic Resonance in Medicine* (2020).
- 620 14. Scherer, T., Sakamoto, K. & Buettner, C. Brain insulin signalling in metabolic  
621 homeostasis and disease. *Nature Reviews Endocrinology* (2021)  
622 doi:10.1038/s41574-021-00498-x.
- 623 15. Dou, W. *et al.* Automatic voxel positioning for MRS at 7 T. *Magn. Reson. Mater.*  
624 *Physics, Biol. Med.* (2015) doi:10.1007/s10334-014-0469-9.
- 625 16. Gruetter, R. & Tkac, I. Field mapping without reference scan using asymmetric echo-  
626 planar techniques. *Magn Reson Med* **43**, 319–323 (2000).
- 627 17. Oz, G. & Tkac, I. Short-Echo, Single-Shot, Full-Intensity Proton Magnetic Resonance  
628 Spectroscopy for Neurochemical Profiling at 4 T: Validation in the Cerebellum and  
629 Brainstem. *Magn Reson Med* **65**, 901–910 (2011).
- 630 18. Bednarik, P. *et al.* Effect of Ketamine on Human Neurochemistry in Posterior

- 631 Cingulate Cortex: A Pilot Magnetic Resonance Spectroscopy Study at 3 Tesla. *Front.*  
632 *Neurosci.* (2021) doi:10.3389/fnins.2021.609485.
- 633 19. Tkac, I., Starcuk, Z., Choi, I. Y. & Gruetter, R. In vivo H-1 NMR spectroscopy of rat  
634 brain at 1 ms echo time. *Magn Reson Med* **41**, 649–656 (1999).
- 635 20. Ridler, T. W. & Calvard, S. Picture Thresholding Using an Iterative Selection Method.  
636 *Ieee Trans. Syst. Man Cybern.* **8**, 630–632 (1978).
- 637 21. Považan, M. *et al.* Automated routine for MRSI data processing. in *2nd TRANSACT*  
638 *Meeting–Quality Issues in Clinical MR Spectroscopy* (2014).
- 639 22. Strasser, B. *et al.* Coil combination of multichannel MRSI data at 7 T: MUSICAL.  
640 *NMR Biomed* **26**, 1796–1805 (2013).
- 641 23. Moser, P. *et al.* Non-Cartesian GRAPPA and coil combination using interleaved  
642 calibration data – application to concentric-ring MRSI of the human brain at 7T. *Magn.*  
643 *Reson. Med.* (2019) doi:10.1002/mrm.27822.
- 644 24. Maudsley, A. A. *et al.* Mapping of brain metabolite distributions by volumetric proton  
645 MR spectroscopic imaging (MRSI). *Magn. Reson. Med.* (2009)  
646 doi:10.1002/mrm.21875.
- 647 25. Hingerl, L. *et al.* Density-weighted concentric circle trajectories for high resolution  
648 brain magnetic resonance spectroscopic imaging at 7T. *Magn. Reson. Med.* (2018)  
649 doi:10.1002/mrm.26987.
- 650 26. Považan, M. *et al.* Mapping of brain macromolecules and their use for spectral  
651 processing of 1 H-MRSI data with an ultra-short acquisition delay at 7 T. *Neuroimage*  
652 **121**, 126–135 (2015).
- 653 27. Gröhn, H. *et al.* Influence of Repetitive Transcranial Magnetic Stimulation on Human  
654 Neurochemistry and Functional Connectivity: A Pilot MRI/MRS Study at 7 T. *Front.*  
655 *Neurosci.* **13**, 1–13 (2019).
- 656 28. Bednařík, P. *et al.* Neurochemical responses to chromatic and achromatic stimuli in  
657 the human visual cortex. *J. Cereb. Blood Flow Metab.* **38**, 347–359 (2018).
- 658 29. Oz, G. *et al.* Clinical Proton MR Spectroscopy in Central Nervous System Disorders.  
659 *Radiology* **270**, 658–679 (2014).
- 660 30. Kreis, R. The trouble with quality filtering based on relative Cramer-Rao lower  
661 bounds. *Magn Reson Med* **75**, 15–18 (2016).
- 662 31. Hangel, G. *et al.* Inter-subject stability and regional concentration estimates of 3D-  
663 FID-MRSI in the human brain at 7 T. *NMR Biomed.* (2021) doi:10.1002/nbm.4596.
- 664 32. Iozzo, P. & Guzzardi, M. A. Imaging of brain glucose uptake by PET in obesity and  
665 cognitive dysfunction: Life-course perspective. *Endocr. Connect.* **8**, R169–R183

- 666 (2019).
- 667 33. Kuehn, B. M. In Alzheimer Research, Glucose Metabolism Moves to Center Stage.  
668 *JAMA* **323**, 297 (2020).
- 669 34. Moser, P. *et al.* Intra-session and inter-subject variability of 3D-FID-MRSI using  
670 single-echo volumetric EPI navigators at 3T. *Magn. Reson. Med.* **83**, 1920–1929  
671 (2020).
- 672 35. De Feyter, H. M. *et al.* Deuterium metabolic imaging (DMI) for MRI-based 3D  
673 mapping of metabolism in vivo. *Sci. Adv.* **4**, eaat7314 (2018).
- 674 36. Lu, M., Zhu, X.-H., Zhang, Y., Mateescu, G. & Chen, W. Quantitative assessment of  
675 brain glucose metabolic rates using in vivo deuterium magnetic resonance  
676 spectroscopy. *J. Cereb. Blood Flow Metab.* **37**, 3518–3530 (2017).
- 677 37. Moser, P. *et al.* Whole-slice mapping of GABA and GABA+ at 7T via adiabatic  
678 MEGA-editing, real-time instability correction, and concentric circle readout.  
679 *Neuroimage* **184**, 475–489 (2019).
- 680 38. Magnusson, P. O. *et al.* Gamma-aminobutyric acid edited echo-planar spectroscopic  
681 imaging (EPSI) with MEGA-sLASER at 7T. *Magn. Reson. Med.* (2019)  
682 doi:10.1002/mrm.27450.
- 683 39. Kullmann, S. *et al.* Dose-Dependent Effects of Intranasal Insulin on Resting-State  
684 Brain Activity. *J. Clin. Endocrinol. Metab.* **103**, 253–262 (2018).
- 685 40. de Graaf, R. A., Thomas, M. A., Behar, K. L. & De Feyter, H. M. Characterization of  
686 Kinetic Isotope Effects and Label Loss in Deuterium-Based Isotopic Labeling Studies.  
687 *ACS Chem. Neurosci.* **12**, 234–243 (2021).
- 688 41. Veltien, A. *et al.* Simultaneous Recording of the Uptake and Conversion of Glucose  
689 and Choline in Tumors by Deuterium Metabolic Imaging. *Cancers (Basel)*. **13**, 4034  
690 (2021).
- 691 42. Plecko, B. *et al.* Oral  $\beta$ -Hydroxybutyrate Supplementation in Two Patients with  
692 Hyperinsulinemic Hypoglycemia: Monitoring of  $\beta$ -Hydroxybutyrate Levels in Blood  
693 and Cerebrospinal Fluid, and in the Brain by In Vivo Magnetic Resonance  
694 Spectroscopy. *Pediatr. Res.* (2002) doi:10.1203/00006450-200208000-00025.
- 695 43. Wang, T. *et al.* Noninvasive assessment of myocardial energy metabolism and  
696 dynamics using in vivo deuterium MRS imaging. *Magn. Reson. Med.* mrm.28914  
697 (2021) doi:10.1002/mrm.28914.
- 698 44. Craft, S. *et al.* The ketogenic diet as a potential prevention or therapeutic strategy for  
699 AD. *Alzheimer's Dement.* (2020) doi:10.1002/alz.038148.
- 700 45. Wright, J. N., Saneto, R. P. & Friedman, S. D. Hydroxybutyrate detection with proton

- 701 MR spectroscopy in children with drug-resistant epilepsy on the ketogenic diet. *Am. J.*  
702 *Neuroradiol.* **39**, 1336–1340 (2018).
- 703 46. Ross, J. M. *et al.* High brain lactate is a hallmark of aging and caused by a shift in the  
704 lactate dehydrogenase A/B ratio. *Proc. Natl. Acad. Sci. U. S. A.* (2010)  
705 doi:10.1073/pnas.1008189107.
- 706 47. Liguori, C. *et al.* CSF lactate levels,  $\tau$  proteins, cognitive decline: A dynamic  
707 relationship in Alzheimer's disease. *J. Neurol. Neurosurg. Psychiatry* (2015)  
708 doi:10.1136/jnnp-2014-308577.
- 709 48. Hyder, F., Fulbright, R. K., Shulman, R. G. & Rothman, D. L. Glutamatergic function  
710 in the resting awake human brain is supported by uniformly high oxidative energy.  
711 *Journal of Cerebral Blood Flow and Metabolism* (2013) doi:10.1038/jcbfm.2012.207.
- 712 49. Hyder, F. & Rothman, D. L. Quantitative fMRI and oxidative neuroenergetics.  
713 *NeuroImage* (2012) doi:10.1016/j.neuroimage.2012.04.027.
- 714 50. Yu, Y., Herman, P., Rothman, D. L., Agarwal, D. & Hyder, F. Evaluating the gray and  
715 white matter energy budgets of human brain function. *J. Cereb. Blood Flow Metab.*  
716 (2018) doi:10.1177/0271678X17708691.
- 717 51. Sundar, L. K. S. *et al.* Towards quantitative [18F]FDG-PET/MRI of the brain:  
718 Automated MR-driven calculation of an image-derived input function for the non-  
719 invasive determination of cerebral glucose metabolic rates. *J. Cereb. Blood Flow*  
720 *Metab.* **39**, 1516–1530 (2019).
- 721 52. Rischka, L. *et al.* Reduced task durations in functional PET imaging with [18F]FDG  
722 approaching that of functional MRI. *Neuroimage* **181**, 323–330 (2018).
- 723 53. Andronesi, O. C. *et al.* Motion correction methods for MRS: experts' consensus  
724 recommendations. *NMR in Biomedicine* (2021) doi:10.1002/nbm.4364.
- 725 54. Dikaios, N., Arridge, S., Hamy, V., Punwani, S. & Atkinson, D. Direct parametric  
726 reconstruction from undersampled (k, t)-space data in dynamic contrast enhanced  
727 MRI. *Med. Image Anal.* (2014) doi:10.1016/j.media.2014.05.001.
- 728 55. Hollingsworth, K. G. Reducing acquisition time in clinical MRI by data undersampling  
729 and compressed sensing reconstruction. *Physics in Medicine and Biology* (2015)  
730 doi:10.1088/0031-9155/60/21/R297.
- 731 56. Yang, A. C.-Y., Kretzler, M., Sudarski, S., Gulani, V. & Seiberlich, N. Sparse  
732 Reconstruction Techniques in Magnetic Resonance Imaging: Methods, Applications,  
733 and Challenges to Clinical Adoption. *Invest. Radiol.* **51**, 349–64 (2016).
- 734 57. Hahn, A. *et al.* Quantification of Task-Specific Glucose Metabolism with Constant  
735 Infusion of 18F-FDG. *J. Nucl. Med.* **57**, 1933–1940 (2016).

- 736 58. Kern, W. *et al.* Low cerebrospinal fluid insulin levels in obese humans. *Diabetologia*  
737 (2006) doi:10.1007/s00125-006-0409-y.
- 738 59. Bingham, E. *et al.* The role of insulin in human brain glucose metabolism. *Diabetes*  
739 (2002).
- 740 60. Seaquist, E. R., Damberg, G. S., Tkac, I. & Gruetter, R. The Effect of Insulin on in  
741 Vivo Cerebral Glucose Concentrations and Rates of Glucose Transport/Metabolism in  
742 Humans. *Diabetes* (2001) doi:10.2337/diabetes.50.10.2203.
- 743 61. Hasselbalch, S. G. *et al.* No effect of insulin on glucose blood-brain barrier transport  
744 and cerebral metabolism in humans. *Diabetes* (1999)  
745 doi:10.2337/diabetes.48.10.1915.
- 746 62. Bednařík, P. *et al.* Hippocampal Neurochemical Profile and Glucose Transport  
747 Kinetics in Patients with Type 1 Diabetes. *J. Clin. Endocrinol. Metab.* **105**, 1–13  
748 (2020).
- 749 63. Rebelos, E. *et al.* Insulin Resistance Is Associated With Enhanced Brain Glucose  
750 Uptake During Euglycemic Hyperinsulinemia: A Large-Scale PET Cohort. *Diabetes*  
751 *Care* (2021) doi:10.2337/dc20-1549.
- 752 64. Talbot, K. *et al.* Demonstrated brain insulin resistance in Alzheimer’s disease patients  
753 is associated with IGF-1 resistance, IRS-1 dysregulation, and cognitive decline. *J.*  
754 *Clin. Invest.* (2012) doi:10.1172/JCI59903.
- 755 65. Kapogiannis, D. *et al.* Dysfunctionally phosphorylated type 1 insulin receptor  
756 substrate in neural-derived blood exosomes of preclinical Alzheimer’s disease.  
757 *FASEB J.* **29**, 589–596 (2015).
- 758 66. Urayama, A. & Banks, W. A. Starvation and triglycerides reverse the obesity-induced  
759 impairment of insulin transport at the blood-brain barrier. *Endocrinology* (2008)  
760 doi:10.1210/en.2008-0008.
- 761 67. Bednarik, P. *et al.* Feasibility of functional spectroscopy on a clinical (3T) scanner,  
762 ESMRMB 2019, 36th Annual Scientific Meeting, Rotterdam, NL, October 3–October  
763 5: Abstracts, Friday. *Magn. Reson. Mater. Physics, Biol. Med.* **32**, 107–233 (2019).  
764